

Use of High-Frequency Seismic Waves for the Detection of Buried Land Mines

Waymond R. Scott, Jr.^a, Seung-Ho Lee^a, Gregg D. Larson^b,
James S. Martin^b, and George S. McCall II^c

^aSchool of Electrical and Computer Engineering

^bSchool of Mechanical Engineering

^cGeorgia Tech Research Institute

Georgia Institute of Technology

Atlanta, GA 30332-0250

ABSTRACT

Over the past three years a system has been under development at Georgia Tech that utilizes a seismic interrogation signal in combination with a non-surface-contacting, radar-based displacement sensor for the detection of buried landmines. Initial work on this system investigated the workability of the system concept. Pragmatic issues regarding the refinement of the current experimental laboratory system into a system which is suitable for field testing and, in turn, one which would be suited to field operations have been largely ignored until recently. Both field operations and realistic field testing require a system that is different from the original laboratory system in two crucial ways. One of these is that a field system needs a sensor standoff from the ground surface larger than the original 1 to 2 cm. This is necessary in order to account for small-scale topography, to avoid ground cover such as grass, and to minimize the risk to the operator. A second difference is that the scanning speed of a field system must be substantially greater than that of the original laboratory system, which takes several hours to image 1 m² of ground surface. From an operational standpoint, the reason for this is obvious. From an experimental standpoint, it is also important because ambient conditions are difficult to control on long time scales outdoors. Both of these new requirements must be met within the design parameters that were established empirically during the development of the laboratory system. One of these is that the system must be capable of measuring peak displacements as small as 1 nm with a 1 Hz resolution band in the low audio frequency range (30 Hz to 2 KHz). This is necessary because of limits placed by the medium on the amplitude of seismic signals that can be generated. Another parameter is that the measurement must be integrated over a region with a diameter of about 2 cm to 5 cm on the ground surface. This is necessary in order to preserve spatial structure of interest for the imaging of small mines. An array of radar-based displacement sensors configured with focused antennas meets all these requirements. A sensor was designed to test this concept. The new sensor was equipped with an antenna consisting of a conical corrugated horn and a bifocal dielectric lens that permitted a 20-cm surface-standoff distance. The sensor was tested in a laboratory experimental model in scenarios similar to those used to evaluate the original system sensor and was found to satisfy all of the new system requirements.

Keywords: land mine, mine detection, seismic waves, focused antenna, radar lens

1. INTRODUCTION

Seismic/elastic techniques for the detection of buried landmines have been under investigation by various groups for more than 30 years.^{1,2} These are promising for the reliable detection of all types of buried mines, even low-metal anti-personnel mines. The reason for this is that mines have unique mechanical properties that can be used to distinguish them from soils and many forms of clutter. Typically, mine components are made from materials that are very stiff in comparison to the surrounding soil. They are also complex mechanical structures with a flexible case, a trigger assembly, air pockets, etc. This complex structure gives rise to structural resonances, non-linear interactions, and other phenomenology that is atypical for both naturally occurring and most types of man-made clutter. Using seismic techniques, this phenomenology can be exploited to distinguish mines from clutter.¹

A seismic mine detection system has been developed at Georgia Tech that uses a radar-based displacement sensor for the local measurement of seismic displacements without physically contacting the soil surface. The non-contact nature of this sensor makes the system capable of interrogating the soil surface near or immediately above a mine.

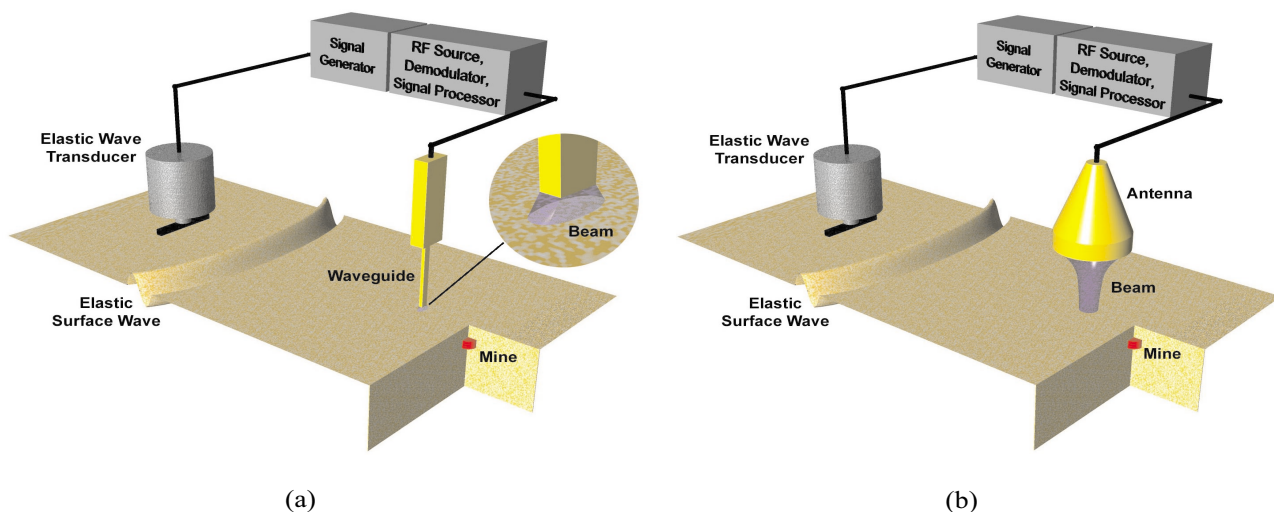
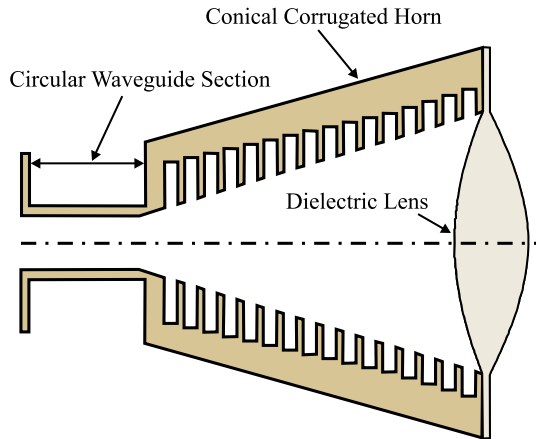


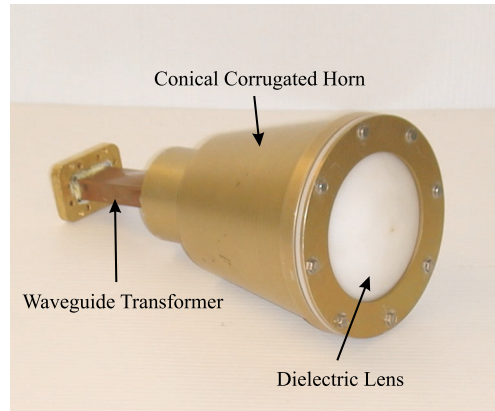
Figure 1. Configuration of laboratory experimental mine detection system: (a) original system and (b) new system.

This substantially increases the measurable effects of the mine's presence over schemes which rely on elastic waves scattered by the mine to propagate to a remote sensor location.² As it is normally configured, this system is depicted in Fig. 1(a). For comparison, the modified system that is currently under investigation is depicted in Fig. 1(b). In both configurations, the source (an electrodynamic shaker resting on a narrow foot) excites an incident signal composed primarily of a Rayleigh surface wave in the 30 Hz to 2 KHz frequency range. This travels across the minefield and excites motion of soil near the surface that includes the buried mines. Deeper soil is not excited by this signal because the Rayleigh wave motion decays exponentially away from the surface of the ground. The transmitted radar signal from the sensor antenna illuminates a spot on the ground surface above the minefield. The reflected radar signal from this spot is phase and amplitude modulated by the seismic surface motions. This modulation, which is proportional to the ground displacement integrated over the spot size, is extracted from the reflected radar signal by analog mixing with a reference signal after it is received. In operation, the sensor is translated to measure surface motion over an array of measurement locations. Sensor data are then stored and post-processed in both space and time domains to yield an image of the minefield.³ In both of the configurations shown in Fig. 1, moving a single sensor forms a synthetic array. A physical array could also be used. This would provide a time saving in proportion to the number of sensors that populate the array. The original sensor (shown in Fig. 1(a)) utilizes an aperture element (an open-ended waveguide) as both a transmitting and a receiving antenna. This is effectively omnidirectional at the 8 GHz operating frequency of the radar sensor. The spot size is kept small (on the order of the 1-cm by 2-cm waveguide dimensions) because the waveguide is in close proximity to the ground (1cm to 2 cm above the surface). The new sensor (Fig. 1(b)) achieves a similar spot size using a focused antenna.

The mine detection system has been tested with the waveguide antenna in laboratory experiments and using numerical models for seismic propagation and scattering. Test conditions have included a variety of inert mines, mine-like targets, realistic clutter objects, and thin organic surface cover. Tests have also been performed in which realistic burial scenarios were simulated. These included trenching from recent mine burials, weathering, and multiple antipersonnel (AP) and antitank (AT) mines buried in close proximity. The results of these experiments, which have been reported in previous papers,^{1,4} show that the system can be used for the detection and imaging of both AT and AP mines over a fairly wide range of realistic conditions. Typical images have shown a contrast between mines and clutter of 20 to 30 dB. Studies have been conducted with this sensor in which the separation of the waveguide and the ground surface was increased well beyond the 1 to 2 cm that was normally used.⁵ In these experiments there was significant degradation in the spatial resolution of the image which could be formed from the experimental data. Digital beamforming techniques were shown to provide some improvement in the spatial resolution with large standoff distances. The problem was also mitigated somewhat by the fact that the image artifacts after beamforming were symmetrically distributed about the actual mine location. They could, therefore, be used to enhance the mine's image in post-processing, provided that there was an a priori knowledge that only one mine was present. Further

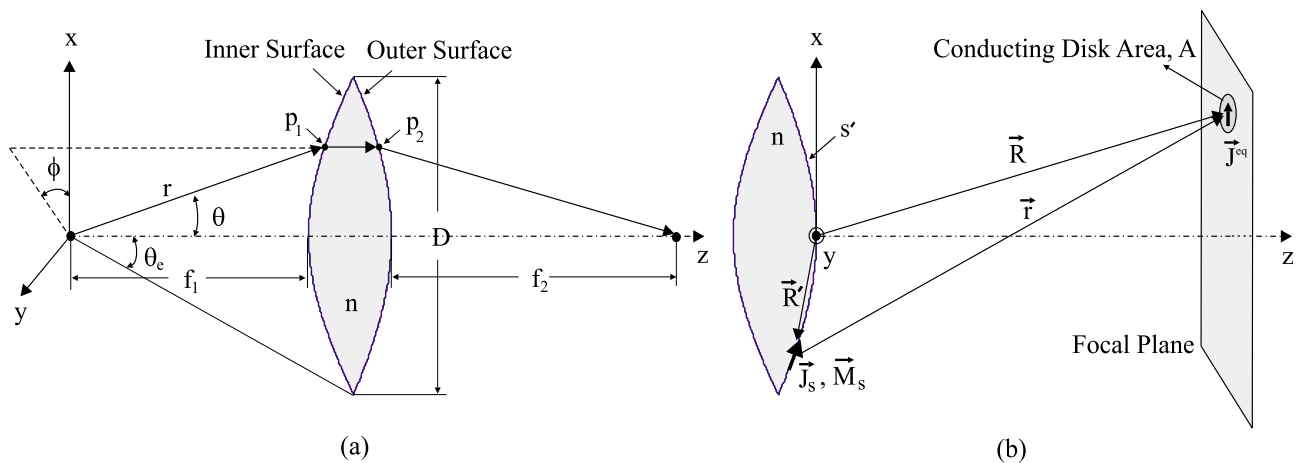


(a)



(b)

Figure 2. The FRD sensor antenna in (a) cutaway and (b) photograph.



(a)

(b)

Figure 3. Geometry of computational model for FRD antenna lens: (a) lens geometry and (b) two-way beam pattern.

substantial improvements in image quality required an unrealistically accurate model for the existing sensor, an impracticably large array of sensors, or an array of more directional sensors. There are many ways in to construct a directional sensor. These include the use of ellipsoidal reflectors, passive microstrip antennas, slotted waveguide antennas, or focusing dielectric lenses. The last of these designs is the one that was pursued and is reported in this paper. It is expected that similar results could be achieved with other design concepts, provided that they were correctly implemented.

2. SENSOR DESIGN

Figure 2 depicts the design of the antenna for the experimental focused radar displacement (FRD) sensor. The antenna consists of a dielectric lens with foci at the surface of the ground and at the open end of a circular waveguide. The lens and the waveguide are connected by a conical metal horn with a corrugated interior. The FRD sensor is monostatic, as its predecessor was, so that this antenna functions as both a transmitter and a receiver.

A theoretical model was constructed for the function of the new antenna. The geometry for this model is shown in Fig. 3. Here the dielectric lens with a refraction index n and a diameter D has two focal lengths, f_1 and f_2 , the inner and the outer focal length, respectively. The diameter of the lens is confined by the semi flare angle (θ_e) of the horn. The inner focal point is assumed to be the same as the phase center of the horn. The inner and outer contours of the lens are hyperbolic curves. The lens profile is rotationally symmetric and is a function of D , f_1 , f_2 , and n . The geometry of the inner surface of the lens is defined as⁶

$$x = r \sin \theta, \quad 0 \leq \theta \leq \theta_e, \quad (1)$$

$$z = \frac{a_1 n + \sqrt{(a_1 n)^2 - (n^2 - 1)(a_1^2 - x^2)}}{n^2 - 1}, \quad (2)$$

where $a_1 = (n - 1)f_1$.

The inner surface of the lens is illuminated by a spherical wave front emanating from the horn. The horn is excited by the TE_{11} mode propagating in the circular waveguide shown in Fig. 2. The TE_{11} mode is converted into the hybrid HE_{11} mode by the discontinuity between the circular waveguide and the horn and facilitated by the corrugations in the horn.⁶ The electric field on the inner surface of the lens can then be described in terms of the geometric parameters by:

$$\vec{E}(\theta, \phi, r) = \left(\frac{P_\nu^1(\cos \theta)}{\sin \theta} + \frac{dP_\nu^1(\cos \theta)}{d\theta} \right) (\cos \phi \hat{\phi} - \sin \phi \hat{\phi}) \frac{e^{-jk_0 r}}{r}, \quad (3)$$

where $P_\nu^1(\cos \theta)$ is the associated Legendre function of the first kind.⁷ ν is determined by the solution of the equation:

$$\frac{P_\nu^1(\cos \theta_e)}{\sin \theta_e} + \frac{dP_\nu^1(\cos \theta_e)}{d\theta_e} = 0. \quad (4)$$

The field on the outer surface of the lens is found by ray tracing. First order reflections from both inner and outer surfaces are considered in this computation by using the Fresnel reflection coefficient. The electric and magnetic surface current densities (\vec{J}_s and \vec{M}_s) on the outer surface can then be determined by an application of boundary conditions and from these the radiation pattern of the lens can be found. The electric and magnetic fields at any point on the focal plane may be represented in terms of the lens's outer surface current densities by the following equations:

$$\vec{E}(\vec{R}) = \frac{-j\omega\mu_0}{4\pi} \iint_{s'} [\vec{J}_s \Psi + \frac{1}{k_0^2} (\vec{J}_s \cdot \nabla') \nabla' \Psi] ds' - \frac{1}{4\pi} \iint_{s'} (\vec{M}_s \times \nabla' \Psi) ds', \quad (5)$$

$$\vec{H}(\vec{R}) = \frac{-j\omega\epsilon_0}{4\pi} \iint_{s'} [\vec{M}_s \Psi + \frac{1}{k_0^2} (\vec{M}_s \cdot \nabla') \nabla' \Psi] ds' + \frac{1}{4\pi} \iint_{s'} (\vec{J}_s \times \nabla' \Psi) ds', \quad (6)$$

where $\Psi = \frac{e^{-jk_0|\vec{r}'|}}{|\vec{r}'|}$ and $\nabla' = \frac{\partial}{\partial x'} \hat{x} + \frac{\partial}{\partial y'} \hat{y} + \frac{\partial}{\partial z'} \hat{z}$. Here, x' , y' , and z' are defined by the coordinate system of the source. The radiated power pattern of the lens-focused corrugated horn is then given by $|\vec{E}(\vec{R})|^2$.

Rather than the radiation pattern of the antenna, it is the two-way beam pattern involving the reflection from a scatterer back to the antenna that is of interest for the determination of the FRD sensor's spot size. This is because the antenna functions as both the radar transmitter and the receiver for the sensor. In order to compute this two-way pattern, a small conducting disk of area A is placed on the focal plane at the location \vec{R} . The surface current on the disk is approximated from the magnetic field defined by Eq. 6. When the disk is electrically small, the electric field at the antenna radiated by the disk is then

$$\vec{E}^r(\vec{R}) = \frac{-j\omega\mu_0}{4\pi} [\vec{J}^{eq} \Psi + \frac{1}{k_0^2} (\vec{J}^{eq} \cdot \nabla) \nabla \Psi] A, \quad (7)$$

where $\vec{J}^{eq}(\vec{R}) = -2\hat{z} \times \vec{H}(\vec{R})$, $\Psi = \frac{e^{-jk_0|\vec{R}|}}{|\vec{R}|}$, and $\nabla = \frac{\partial}{\partial x} \hat{x} + \frac{\partial}{\partial y} \hat{y} + \frac{\partial}{\partial z} \hat{z}$.

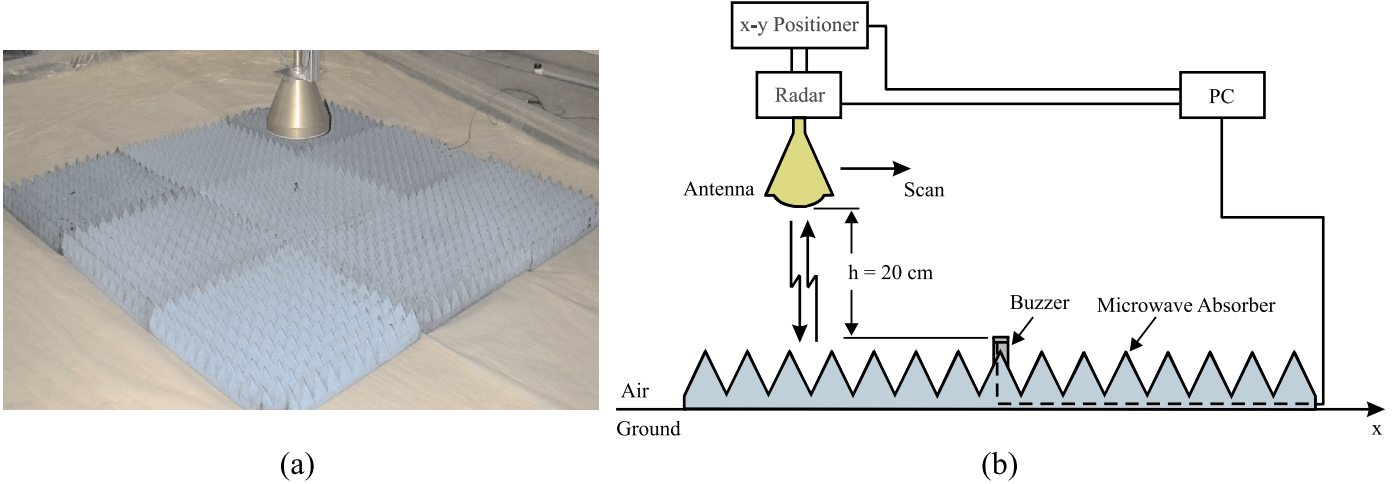


Figure 4. FRD sensor directivity measurement: (a) photograph and (b) schematic.

The voltage received by the antenna from each of the secondary sources is found to be:

$$V^r(\vec{R}) = \vec{E}^r(\vec{R}) \cdot \vec{l}^e(\vec{R}), \quad (8)$$

where \vec{l}^e is the effective height of the antenna, which can be determined by the antenna's radiated field as computed in Eq. 5 to be⁸:

$$\vec{l}^e(\vec{R}) = \alpha \frac{4\pi|\vec{R}|\vec{E}(\vec{R})}{-j\eta_0 k_0 e^{-jk_0|\vec{R}|}}, \quad (9)$$

where α is a proportional constant that depends on the details of how the antenna is fed. The two-way pattern is then obtained from $|V^r(\vec{R})|^2$.

If the lens were illuminated by a spherical wavefront with uniform amplitude, strong side lobes would be expected in its two-way beam pattern. The corrugations on the interior of the conical horn were designed so as to ameliorate these by tapering the amplitude of the electric field near the edges of the lens. The corrugations were designed using standard procedures for this type of device.⁶ The width of the corrugations is less than $\frac{\lambda_c}{2}$. The depth of the slots is between $\frac{\lambda_c}{4}$ and $\frac{\lambda_c}{2}$. The slot depths taper from $\frac{\lambda_c}{2}$ near the throat of the horn to $\frac{\lambda_c}{4}$ at the aperture with the variation occurring on a scale which is large compared to the wavelength. As it was designed and built, the prototype antenna had the same inner and outer focal distances, both of which were 20 cm. This created a plane of symmetry for the lens and provided some fabrication convenience but was not required for the design.

3. SENSOR EVALUATION

In order to measure the spot size of the FRD sensor, an experiment was conducted in which a small piezoelectric buzzer was placed in the center of a 1.8 m by 1.8 m anechoic surface. The buzzer was driven at 1KHz, and the sensor output was recorded at this frequency using a two-second-integration time to build dynamic range above the noise floor. The antenna was then translated linearly across the surface. From a system standpoint, an ideal sensor under these circumstances would have measured only the displacement of the buzzer when it was directly above the buzzer and zero elsewhere. The anechoic treatment assured that the measurement could not be contaminated by ambient vibration and by single and multiple reflected signals from the ground and the buzzer. The configuration of this experiment is depicted in Fig. 4.

The results of the directivity experiment are shown in Fig. 5. The 3dB beam width on the ground was found to be about 4.7 cm. The beam pattern was well predicted by theory for horizontal sensor offsets up to about 15 cm. Beyond 15 cm the FRD sensor consistently outperformed model predictions. This result is difficult to explain. The antenna may actually perform better than predicted due to inaccuracies in the model, or it may be an inaccuracy in the measurement. The measurement inaccuracy could be due to abnormal motion of the buzzer, such as horizontal

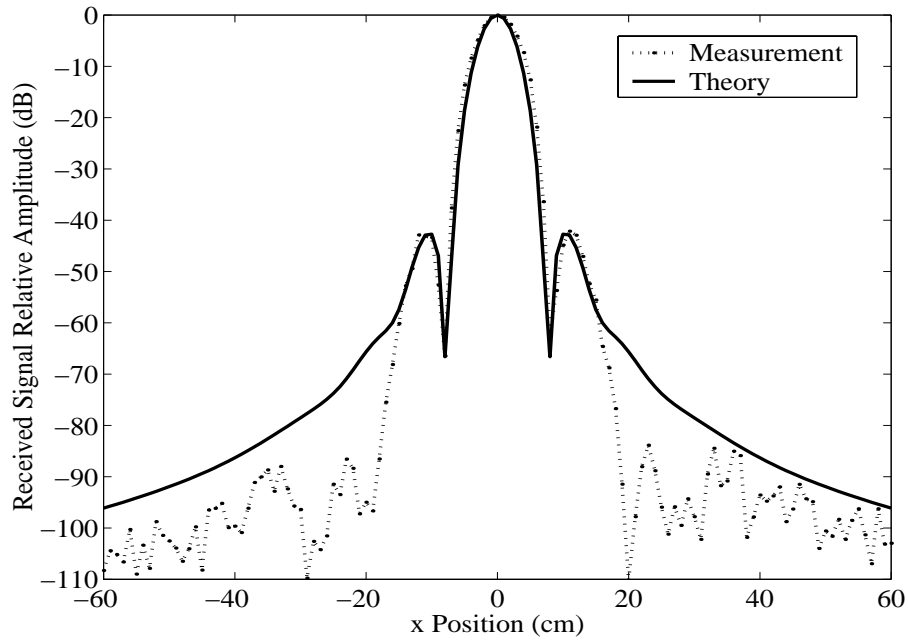


Figure 5. Results of FRD sensor directivity measurement.

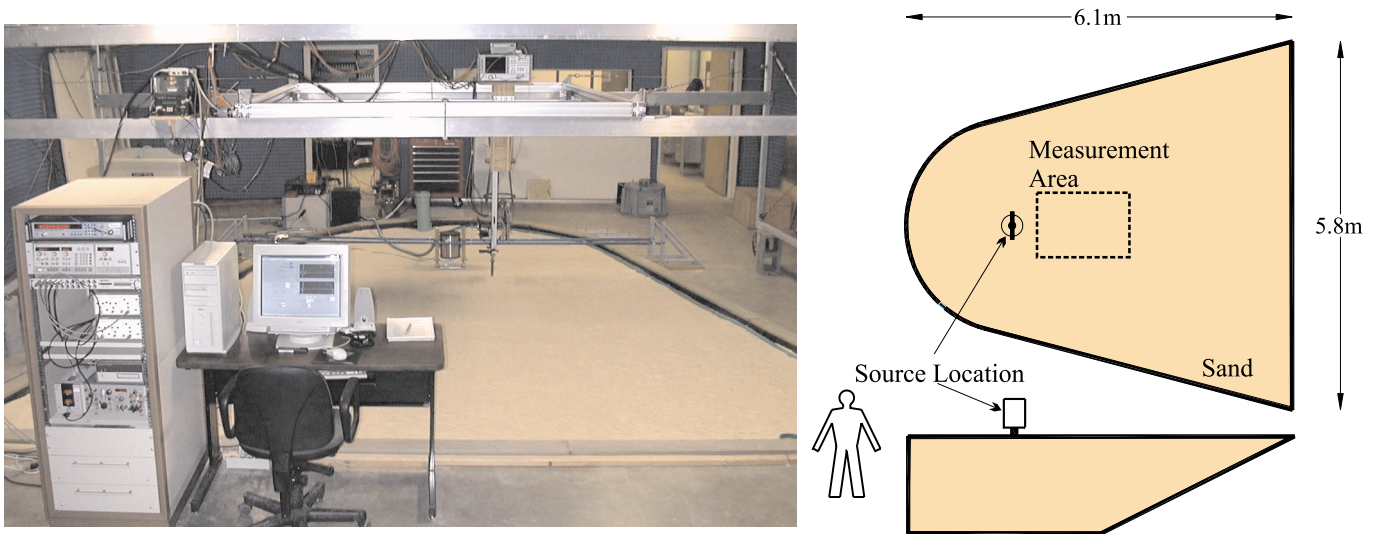


Figure 6. The laboratory experimental model.

motion of its case, which adds destructively with the motion sensed from the radiating surface on the top of the buzzer. Since the FRD sensor only responded to motion in the direction of the EM propagation path, it would be insensitive to this lateral motion when it was directly above the buzzer. The relative contribution of this motion to the sensor output would have increased as the antenna was translated away from the buzzer, and the EM path became more horizontal.

4. LABORATORY EXPERIMENTS

The FRD sensor was tested in the laboratory model that was used for the development of the mine detection system. This model is depicted in Fig. 6. It is a wedge-shaped tank filled with over 50 tons of damp compacted sand to simulate soil. The seismic source is located near the tip of the wedge and is bi-directive toward the search area and the back wall. Simulated mines, inert mines, and clutter, such as rocks and sticks, are buried within a 2-m-by-2-m region in the center of the tank. The FRD sensor was scanned above this region with a three-degree-of-freedom positioner fixed to a framework above the tank. This was done using a typical two-dimensional scan that covers an 80-cm by 120-cm boundary-inclusive area. It is sampled in 1-cm increments along the direction of seismic wave propagation, from 30 cm to 150 cm out from the source. 2-cm increments are sampled across the seismic wave fronts (out to 40 cm on either side of the plane of symmetry, apparent in the top view of the model in Fig. 6). A total of 4,961 measurement locations were sampled in this scan before an image was formed. These scan parameters were arrived at during work with a smaller experimental model. The search dimensions have not been increased in most of the work with the larger model in order to save time. Since there is currently a four-second dwell over each measurement location used to build up the signal-to-noise ratio in the received signal, even the current 1 m² scan requires 7 hours to complete. In addition to building an array of sensors, reducing the dwell time and increasing the scan increments are being considered to speed a field-operable system. The 1 cm and 2 cm scan increments used in the measurements are clearly smaller than necessary since the antenna averages the displacement over a region of the ground with a diameter of about 4.7 cm. These scan increments were used to make comparisons with previous data easier.

Four-second displacement time histories are acquired with 8-KHz sampling and 12-bit resolution for each measurement location and stored as frequency domain transfer functions between the source's drive signal and the sensor's received signal. This must ultimately be reduced to a single image which depicts the probability of a buried mine below each location on the planar surface. There are many ways in which this sort of post processing can be performed. The scheme that is currently employed has been described in a previous paper.³ The technique involves a multi-step process that exploits observed features of mine response, such as localized resonance effects, to enhance the background contrast in the final image. First the response of the system to a differentiated Gaussian pulse, which typically has a center frequency of 450 Hz, is synthesized from the recorded transfer functions. The data are then filtered temporally and spatially to remove low and high frequency noise. The forward-propagating waves (waves travelling away from the source) are then filtered out in k-space, leaving only the back-scattered waves. Two data sets are created from the remaining time histories. The first data set is the energy at each spatial position in the back-scattered waves at times of arrival near the incident wave. The second data set is the energy that propagates back toward the seismic source from each spatial position. Taking the product of these two data sets forms the final image. Nothing about the displacement sensing mechanism is presumed in this scheme other than that the measurements represent true point displacements. Thus, no modifications to the imaging scheme were made to accommodate the FRD sensor. This provided the additional advantage of allowing direct comparison with existing images in the evaluation of sensor performance.

5. AP MINE DETECTION AND IMAGING

Two mine-imaging experiments were performed to evaluate the FRD sensor. In the first of these a single TS-50 AP mine was buried with its top-most surface 1 cm below the sand in the center of the scan region. The sand surrounding the mine was carefully repacked after the burial to simulate the effects of weathering. This is a baseline configuration, which has been tested many times with other sensor types and in other experimental models for comparison purposes.^{1,9} The minefield was then covered with a 15-cm layer of pine straw to simulate realistic organic ground cover. This is similar to earlier experiments in which 2-cm to 3-cm layers of pine straw were used in testing with the waveguide antenna. The thickness of pine straw covering the scan region was increased to 15 cm because the greater standoff of the FRD sensor permitted this. Figure 7 shows a comparison between a scan performed with the waveguide antenna 1 to 2 cm high (Fig. 7(a)) and the two scans performed with the FRD antenna 20 cm high: one without the pine straw (Fig. 7(b)) and one with the pine straw (Fig. 7(c)). It is clear from the data presented in the figure that the FRD sensor images this relatively small AP mine with an image contrast comparable to the sensor that is equipped with the waveguide antenna. Unlike earlier attempts to implement digital beamforming arrays of omnidirectional sensors,⁵ the image shows no artifacts that are remote from the actual mine location. However, the spatial resolution is somewhat less than with the waveguide antenna; this is expected since the FRD antenna averages the displacement over a somewhat larger area than does the waveguide antenna. In either

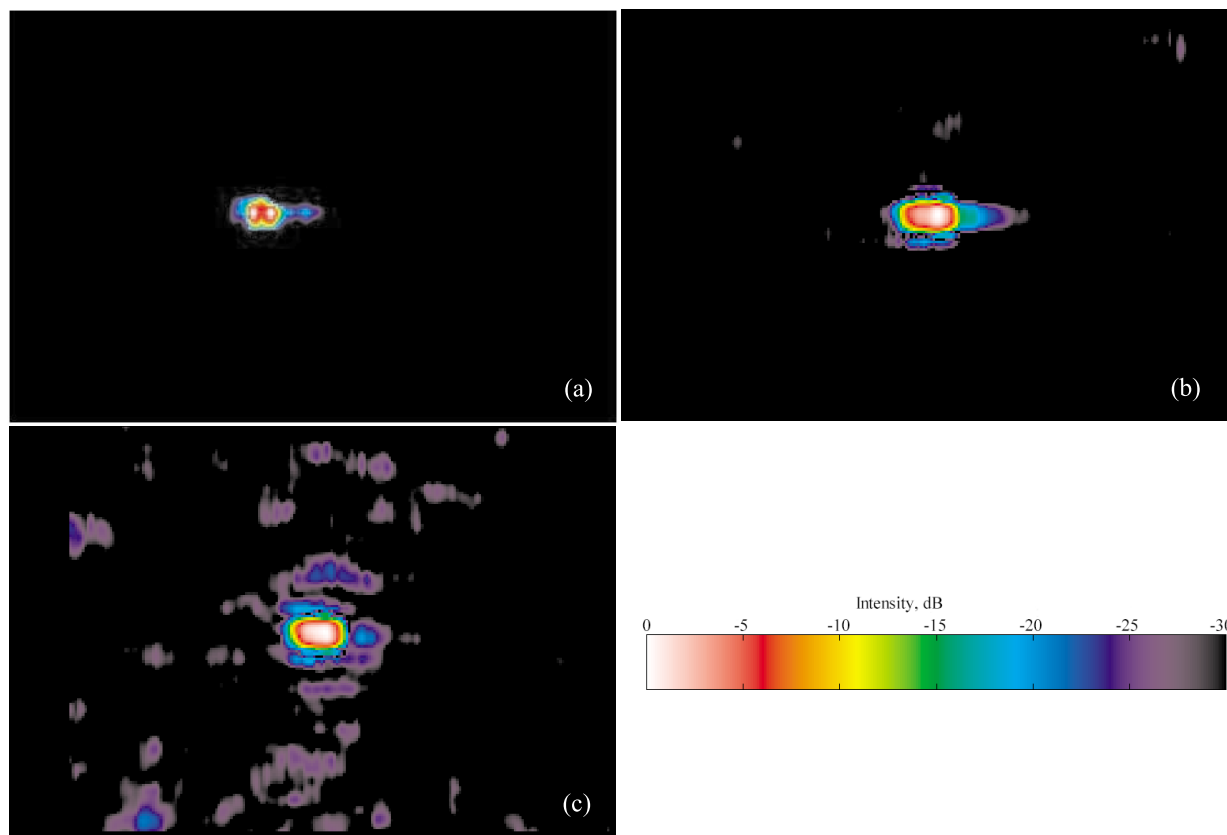


Figure 7. Images formed from two-dimensional scans above a TS-50 mine buried 1cm deep: (a) using the waveguide antenna, (b) using the FRD sensor over a clean surface, and (c) using the FRD sensor over 15 cm of pine straw.

event, the image shows more than adequate spatial resolution for operational purposes when one considers the 120-cm by 80-cm scale on which it is depicted. Further research is planned to determine the appropriate spatial resolution for the sensor: higher spatial resolution yields a higher fidelity image but at the cost of slower measurement times because the higher spatial resolution will necessitate smaller scan increments. The ground cover seems to introduce some clutter into the image, but this is more than 25 dB below the level of the mine image. The source of this clutter is not currently known: It may be due to pine straw or it may be due to an increase in environmental noise for this particular measurement. Previous attempts to quantify the effects of ground cover were confounded by the small standoff distance of the waveguide sensor.¹ There is, therefore, no appropriate data for comparison with the FRD sensor's performance. The fact that this measurement was even possible makes a favorable statement regarding the FRD sensor's design.

6. MULTIPLE MINE IMAGING

The most challenging burial scenario that can be simulated in the experimental model is the detection of both AP and AT mines in close proximity to each other and in the presence of buried clutter. This is a realistic scenario, since it is a common practice of mine warfare to plant multiple AP mines in close proximity to AT mines. The AP mines thereby protect the AT mine from sappers who can more easily detect the larger object and remove it with little personal danger. This poses a unique detection problem in that it requires a system to operate with sensitivity appropriate to both mine types simultaneously. Also, the system must be capable of distinguishing individual targets and rejecting ghost images formed by multiple-scattering effects. This scenario has been previously investigated using the waveguide antenna, which was found to offer adequate spatial resolution to image all of the buried mines with a reasonable set of parameters selected for the installation.¹ The FRD sensor was tested over a similar burial arrangement. The layout of this experiment and the relative scale of the buried objects can be seen in Fig. 8. The

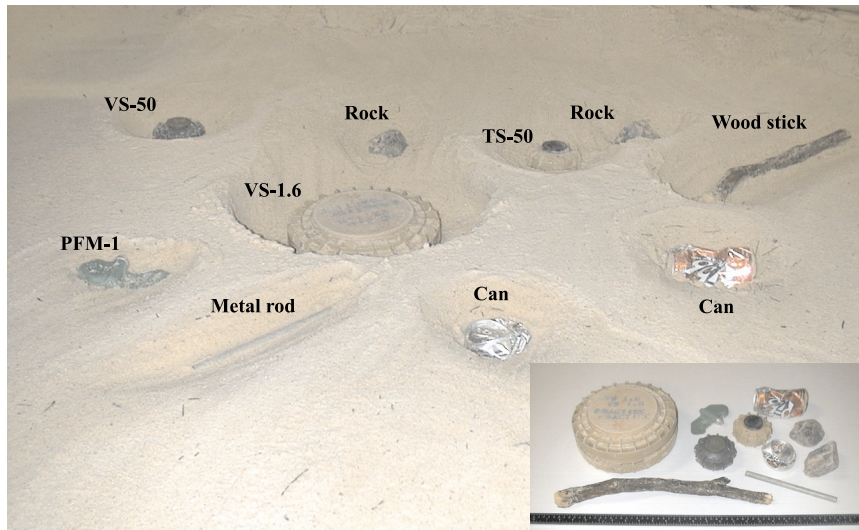


Figure 8. Photograph showing the multiple mine burial uncovered and the relative scale of the buried objects (insert).

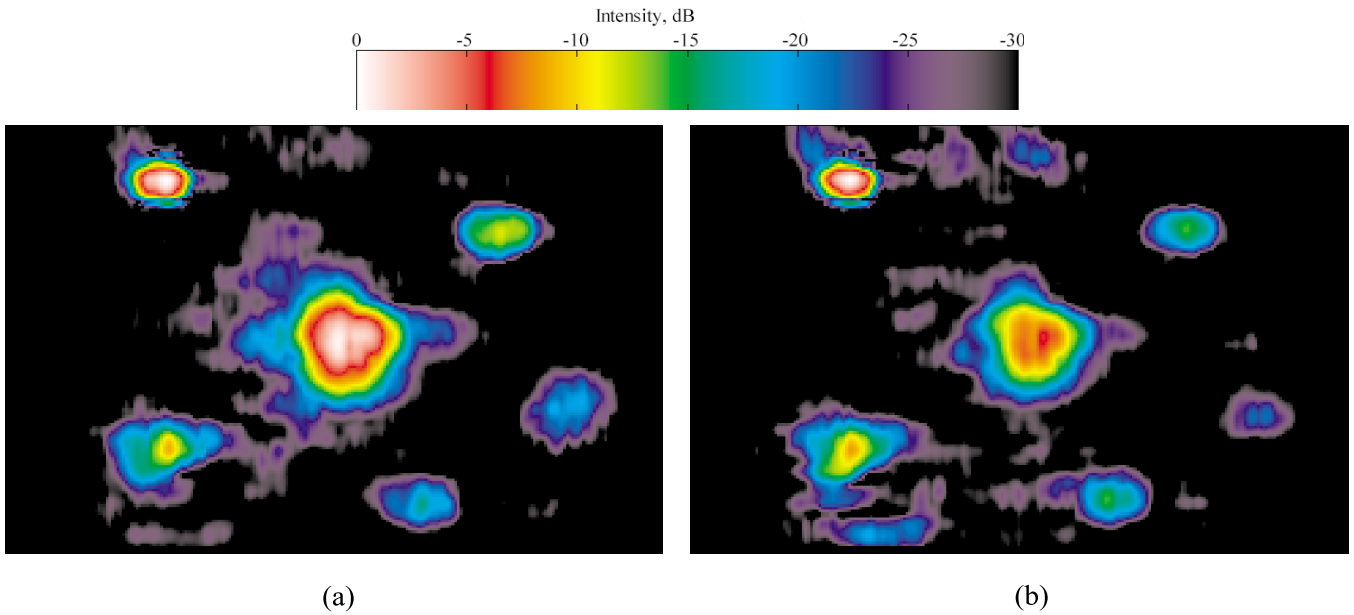


Figure 9. Images formed of multiple mine burial using the FRD sensor: (a) clean scan and (b) with 15 cm of pine straw.

AT mine was a VS-1.6. Three AP mines surrounded it: a TS-50, a VS-50, and a PFM-1. The clutter objects included two AP mine-sized rocks, two aluminum beverage cans, a steel rod, and a large stick. As before, the minefield was covered with a layer of pine straw 15 cm thick, and the sand was carefully packed around all of the buried objects. Figure 9 shows the image that was formed of this burial with and without the 15 cm of pine straw. All of the mines are clearly visible in this image. Note that the image with the pine straw is comparable to that without the pine straw for this case: it does not have the increased clutter visible in Fig. 7. In addition to the mines, the beverage cans also show up well in the image. This is because they are air-filled and therefore exhibit low-frequency structural resonances similar to those that identify the mines. This type of clutter could easily appear as a mine to the current seismic imaging algorithm much as it would fool an individual using a metal detector. In contrast, the steel rod

would also have fooled the metal detector but is not imaged using the seismic system. This provides an illustration of how multiple sensor types might be exploited for the reduction of false alarms in a field-operational system.

7. CONCLUSIONS

A seismic mine detection system has been tested in a laboratory experimental model. The system is similar to one that has been described in previous papers^{1,3,4,9} but was outfitted with a focused-radar displacement (FRD) sensor. The FRD sensor replaced an earlier sensor equipped with an open-ended waveguide antenna that needed to be located 1 to 2 cm above the ground in order to achieve sufficient spatial resolution for mine detection. The FRD sensor, which is based on a dielectric lens and corrugated horn design, allows the system to stand off 20 cm from the ground surface while achieving detection and imaging performance comparable to the earlier design. This sensor addresses the standoff requirements of a field operable system. In conjunction with other planned hardware and software improvements, an array of these sensors should also address the scanning speed requirements of such a system. Future plans for the development of the system involve building a small array of these sensors and transitioning the experimental work into outdoor testing.

ACKNOWLEDGMENTS

This work was supported in part by the US Army Night Vision Electronic Systems Directorate, S&T Division, Countermine Technology Team and by the OSD MURI program by the US Army Research Office under contract DAAH04-96-0448.

REFERENCES

1. W. R. Scott, Jr., J. Martin, and G. Larson, "Experimental model for a seismic landmine detection system," *IEEE Transactions on Geoscience and Remote Sensing*, to appear July 2001.
2. *Feasibility of Acoustic Landmine Detection: Final Technical Report*, BBN Technical Report NO. 7677, May 1992.
3. A. Behboodian, W. R. Scott, Jr., and J. H. McClellan, "Signal processing of elastic surface waves for localizing buried land mines," *Proceedings of the 33rd Assilomar Conference on Signals, Systems, and Computers*, Assilomar, CA, October 1999.
4. W. R. Scott, Jr., G. Larson, and J. M. and, "Simultaneous use of elastic and electromagnetic waves for the detection of buried land mines," *Proceedings of the SPIE: 2000 Annual International Symposium on Aerospace/Defense Sensing, Simulation, and Controls*, Orlando, FL, Vol. 4038, pp. 667-678, April 2000.
5. S. H. Lee and W. R. Scott, Jr., "Near-field beamforming array for detecting elastic waves in the earth," *Proceedings of the SPIE: 2000 Annual International Symposium on Aerospace/Defense Sensing, Simulation, and Controls*, Orlando, FL, Vol. 4038, pp. 691-699, April 2000.
6. Y. T. Lo and S. W. Lee, *Antenna Handbook: Antenna Theory*, Van Nostrand Reinhold, New York, 1993.
7. G. B. Arfken and H. J. Weber, *Mathematical Methods for Physicists*, Academic Press, 1995.
8. C. A. Balanis, *Antenna Theory: Analysis and Design*, John Wiley and Sons, 1997.
9. W. R. Scott, Jr. and J. Martin, "Experimental investigation of the acousto-electromagnetic sensor for locating land mines," *Proceedings of the SPIE: 1999 Annual International Symposium on Aerospace/Defense Sensing, Simulation, and Controls*, Orlando, FL, Vol. 3710, pp. 204-214, April 1999.